Advanced Composite Materials
Publication details, including instructions for authors and subscription information:
http://www.tandfonline.com/loi/tacm20

Thermal Fatigue Behavior of 3D-Woven SiC/SiC Composite with Porous Matrix for Transpiration Cooling Passages

Toshimitsu Hayashi [a] & Shuichi Wakayama [b]

[a] Department of Mechanical Engineering, Tokyo Metropolitan University, 1-1 Minami-Ohsawa, Hachioji-shi, Tokyo 192-0397, Japan;, Email: hayashi-toshimitsu@ed.tmu.ac.jp

[b] Department of Mechanical Engineering, Tokyo Metropolitan University, 1-1 Minami-Ohsawa, Hachioji-shi, Tokyo 192-0397, Japan

Version of record first published: 02 Apr 2012.

To cite this article: Toshimitsu Hayashi & Shuichi Wakayama (2009): Thermal Fatigue Behavior of 3D-Woven SiC/SiC Composite with Porous Matrix for Transpiration Cooling Passages, Advanced Composite Materials, 18:1, 61-75

To link to this article: http://dx.doi.org/10.1163/156855108X379354

VSP

Advanced Composite Materials 18 (2009) 61–75

ADVANCED COMPOSITE MATERIALS
www.brill.nl/acm

Thermal Fatigue Behavior of 3D-Woven SiC/SiC Composite with Porous Matrix for Transpiration Cooling Passages

Toshimitsu Hayashi * **and Shuichi Wakayama**

Department of Mechanical Engineering, Tokyo Metropolitan University, 1-1 Minami-Ohsawa, Hachioji-shi, Tokyo 192-0397, Japan

Received 21 August 2008; accepted 10 September 2008

Abstract

The effect of porous matrix on thermal fatigue behavior of 3D-orthogonally woven SiC/SiC composite was evaluated in comparison with that having relatively dense matrix. The porous matrix yields open air passages through its thickness which can be utilized for transpiration cooling. On the other hand, the latter matrix is so dense that the air passages are sealed. A quantity of the matrix was varied by changing the number of repetition cycles of the polymer impregnation pyrolysis (PIP). Strength degradation of composites under thermal cycling conditions was evaluated by the 1200°C/RT thermal cycles with a combination of burner heating and air cooling for 200 cycles. It was found that the SiC/SiC composite with the porous matrix revealed little degradation in strength during the thermal cycles, while the other sample showed a 25% decrease in strength. Finally it was demonstrated that the porous structure in 3D-SiC/SiC composite improved the thermal fatigue durability.

Keywords

Ceramics matrix composite, thermal fatigue, transpiration cooling, polymer impregnation pyrolysis, burner rig test, micro-focused X-ray CT scan, SiC fiber

1. Introduction

It has been desirable that ceramic matrix composites (CMCs) will replace conventional Ni-based alloys as the hot section members of aircraft jet engines in order to enhance the heat resistance. The greater the available heat resistance is, the higher is the engine operating temperature or the smaller the supplied cooling-air, both of which significantly increase the thrust of jet-engines. In addition, their relatively low density, which is approximately 70% lower than the Ni-based alloys, is attractive in producing weight reduction of jet engines. From the point of practical use, even if the Ni-based alloys are replaced with the CMCs, active cooling is still re-

* To whom correspondence should be addressed. E-mail: hayashi-toshimitsu@ed.tmu.ac.jp
Edited by the JSCM

 DOI:10.1163/156855108X379354

quired to reduce both convection and radiation heat transfer to preserve structural strength, since the temperature capability of the CMCs is still lower than the hot gas temperature (e.g., 1600°C at turbine inlet).

The machined cooling holes have been conventionally applied to Ni-based alloys. However, they are inapplicable to the CMCs, because machined holes damage fibers and thus decrease the nominal strength of the CMCs. Cox *et al*. suggested that air cooling holes penetrated through thickness can be fabricated in textile composites by repositioning the fiber yarns during the textile fabrication process [1]. Although the cooling holes can be fabricated without breaking fibers, the penetrated cooling holes would not provide large enough area of inner wall to transfer heat from material to the cooling air. To save cooling air, it is necessary to enhance the efficiency of the heat transfer to the cooling air. For this purpose, fine cooling channels should be created, such as with porous materials. The cooling method that utilizes fine cooling channels of porous material is called 'transpiration cooling', which is one of the most effective cooling methods [2].

Some porous ceramics with open-cell structure [3–5] may achieve transpiration cooling using connected porosities. However, they are inadequate for the jet-engine structural parts due to their spalling behavior [3] that results in domestic object damage, and the range of applications is strictly limited due to significantly low mechanical strength [3–5].

In this study, the transpiration cooling structure was created in the 3D-woven SiC fiber-reinforced composite with SiC matrices derived from both chemical vapor infiltration (CVI) and polymer impregnation pyrolysis (PIP). The PIP–SiC matrix was reduced in order to form large cavities, and then the cooling passage can be created through the cavities, without fiber breakage. This method can retain the static mechanical strength. The purpose of this study was to investigate the effect of the transpiration structure (i.e., porous structure) on the thermal fatigue behavior. Burner rig tests were carried out to investigate the thermal fatigue behavior, and the strength degradation due to the thermal fatigue was evaluated by measuring the change in bending strength. The influence of the porous structure will be discussed in this paper.

2. Experimental

2.1. Materials and Specimens

The weaving structure of the SiC/SiC composite used in this study is three-dimensional (3D) orthogonal with a 2 mm pitch in 7 layers as schematically shown in Fig. 1. The SiC fibers used are Tyranno™ ZMI (Ube Industries Ltd., 1600 filaments per yarn). The fiber content ratio along the X, Y and Z axes is 1:1:0.2 (volume fraction ratio is 18%:18%:4%), respectively. The woven preforms were coated with a carbon interface by the CVI process to control the fiber/matrix interfacial shear strength.

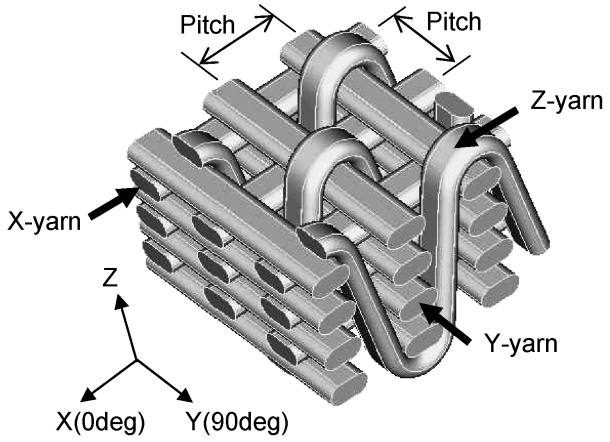

Figure 1. Schematic of 3D-orthogonal weaving architecture (Fiber: Tyranno ZMI SiC fiber, fiber contents; $X{:}Y{:}Z = 1{:}1{:}0.2$, 1600 filaments per yarn).

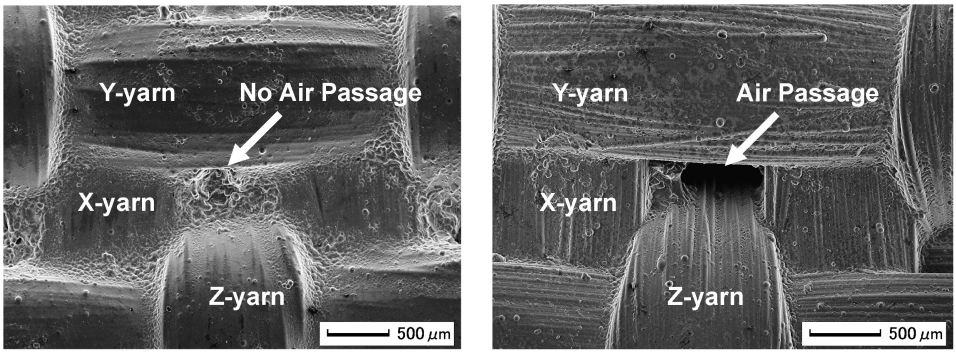

(a) (b)

Figure 2. SEM micrographs showing the surface morphology of (a) 3D-H and (b) 3D-L.

Successively, the preforms of 200 mm × 100 mm were densified with SiC derived from methyltrichlorosilane by the CVI process and from polycarbosilane by the PIP process [6]. The porosity was controlled by varying the number of PIP cycles. The 3D fabrics after 4 PIP cycles and 9 PIP cycles were denoted as specimens 3D-L and 3D-H, respectively. Following the PIP treatments, the specimens were cut into 50 mm squares and coated with a layer of CVI–SiC of ∼10 μm in thickness to protect the surface from oxidation. The thickness of specimens 3D-L and 3D-H were ∼2 mm. Figure 2 shows SEM micrographs of the surface morphology of specimens 3D-H and 3D-L. It can be seen in the figure that an open pore for a cooling passage was observed only in 3D-L. Table 1 shows detailed volume fractions of the specimens. The matrix volume fractions in the table were calculated by the matrix density (∼2 g/cm^3) and the matrix weight measured before and after the densification of the matrix. The porosity of 3D-L was ∼10% higher than that of 3D-H.

Table 1.
Volume fractions of test specimens (averaged value in 200 mm × 100 mm panel)

Specimen	Fiber V_f (%)	Matrix V_m (%)	Porosity V_p (%)
3D-L	40	34	26
3D-H	40	45	15

Table 2.
Mechanical and thermal properties of specimen 3D-L and 3D-H

Specimen	3D-L	3D-H
Elastic modulus (GPa)		
20°C	97	109
1000°C	90	103
Coefficient of linear expansion $\times 10^{-6}$ ($°C^{-1}$)		
1250°C	5.8	5.6
Thermal conductivity ($W \cdot m^{-1} K^{-1}$)		
25°C	3.55	3.67
1200°C	3.78	3.90

Mechanical and thermal properties are shown in Table 2. The data will be used to discuss thermal stress and temperatures of specimens during burner rig tests. Elastic modulus was measured by flexural resonance method (Nippon Techno-plus: EG-HT). A thermal mechanical test machine (Shinkuriko, TM 3000) was used to measure the coefficient of in-plane thermal expansion. Thermal conductivity along the thickness direction was obtained by the laser flash method (Shinkuriko: TC-7000) using disc-shaped specimens of 10 mm in diameter and 1 mm in thickness.

2.2. Air Flow Test

Air flow characteristics of specimen 3D-L and 3D-H were investigated by the air flow test. Figure 3 schematically shows the testing apparatus. Nitrogen gas was used to create a differential pressure of 5 kPa at maximum. The lowest working pressure of the gauge was 0.01 kPa. Four specimens with the dimensions of 50 mm square and ∼2 mm thickness were prepared from the same lot and subjected to the air flow test. The specimens were mounted using oil-based clay, because air-tightness around the edges of the specimen was required to increase the differential pressure.

2.3. Micro-focused X-ray CT Scan Inspection

The geometry of cooling passages formed within the specimens was observed using a micro-focused X-ray CT scan (Toshiba IT control, Toscanner-32250μhd) [7].

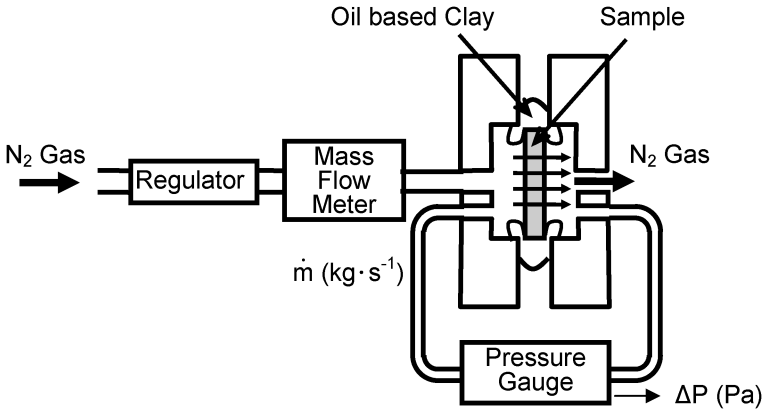

Figure 3. Schematic of the air flow test (gas pressure: 0–5 kPa, gas temperature: RT).

The specimens were prepared to be within ⌀10 mm. Slice images in X–Y plane were captured by a pitch of 0.02 mm along the Z-axis, which required almost one hundred micrographs for each specimen.

2.4. Burner Rig Test

Burner rig tests were carried out using the experimental set-up, schematically shown in Fig. 4. The front surface of the specimen of 50 mm square was heated for 2 min using a gas furnace at a temperature of 1700°C. The gas burner utilized a mixture of methane gas of 45 l/min and oxygen gas of 110 l/min. Following the heating, the surface of specimens was quickly cooled down to room temperature by two additional air jets of 60 l/min from the burner side for 3 min in order to simulate shutdown of the gas turbine. Thermal cycle of the heating for 2 min and cooling for 3 min was repeated 200 times. Front surface temperatures were monitored by three pyrometers (Japan Sensor Co., FTZ2-A600) targeted at three points of the specimen (two diagonal corners and center). The target size of pyrometers was about 5 mm in diameter.

Figure 5 shows the sample holder schematically. Each specimen was supported at four sides using ceramic pins. The backside surface temperatures were measured by five spring-loaded thermocouples of type-K at four corners and center of the specimen. Cooling air of 40 l/min at room temperature and cooling water were continuously supplied to protect the holder from heat damage. The rear surface of the specimen was also cooled by the air, which generated a thermal gradient along the thickness direction in a similar manner to that in jet-engine hot sectional applications. However, in the test facility it was difficult to increase backside pressure for transpiration cooling, because the flow of cooling air from backside of the specimen cannot be blocked in order to protect the specimen holder.

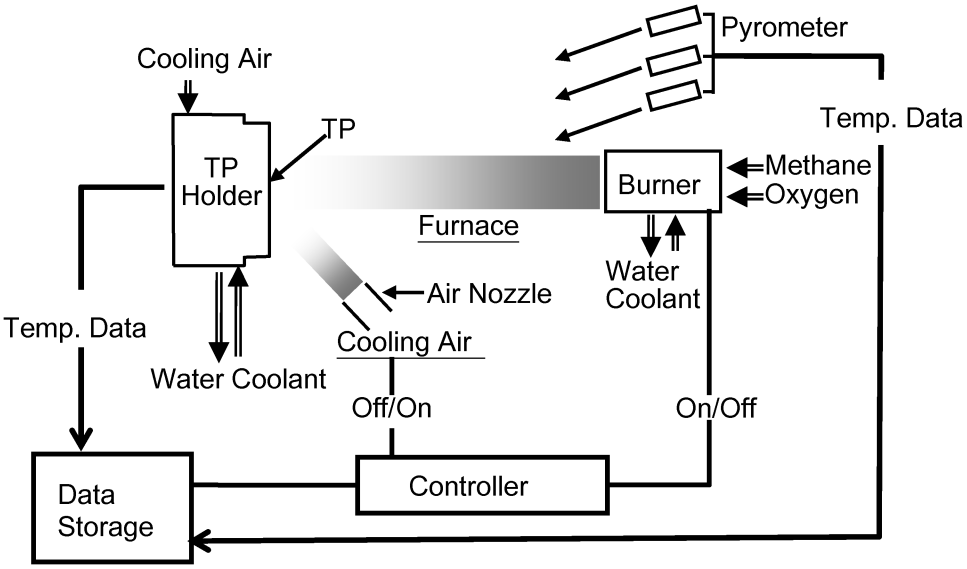

Figure 4. Schematic overview of burner rig test system.

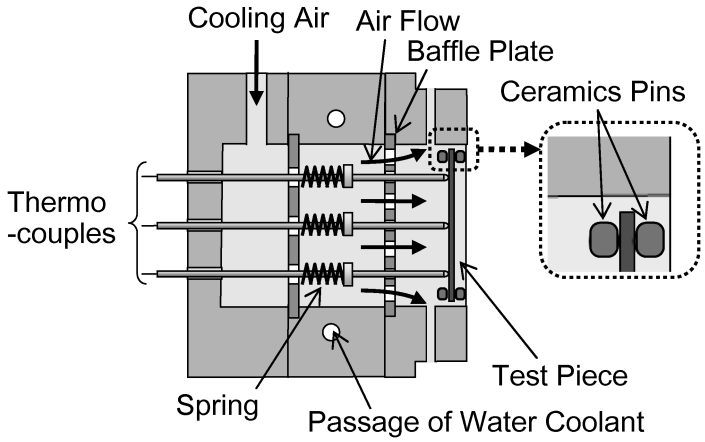

Figure 5. Schematic of set-up of specimen.

2.5. Bending Test

The bending test was carried out to evaluate the strength degradation due to thermal fatigue. Bending strengths were measured by 4-point bending with a loading span of 10 mm and a supporting span of 30 mm at room temperature in air under a constant displacement speed of 0.5 mm/min. The dimensions of the specimen were 50 mm in length, 4 mm in width and ~2 mm in thickness. The width is equivalent to the size of 2 pitches of the textures. Four specimens were prepared by cutting from the center location of the specimen after the burner rig test. The burner-side surface was subjected to tensile stress during bending tests. Additionally, ten specimens of

3D-H and 3D-L were cut out from virgin samples of 50 mm square to obtain the initial strength.

3. Results and Discussions

3.1. Air Flow Characteristics

Air flow tests were conducted to confirm the air-permeability and measure the air flow rates. Figure 6 shows the mass flow rates *versus* $\Delta P/P$ for 3D-L and 3D-H, where P is the chamber pressure and ΔP is the differential pressure. The open circles in the figure indicate the data obtained from four same-lot samples of 3D-L, while solid circles indicate the data for 3D-H. The mass flow rates of the samples of 3D-L increase with the differential pressure $\Delta P/P$. This result demonstrates the existence of open channels, which enables the transpiration cooling in the composites 3D-L. However, the flow characteristic exhibited large scatter, which may be attributed to micro-structural variations among specimens. On the other hand, air flow was not observed in any specimens of 3D-H. The results also suggest that the flow rate of the composites can be controlled by selecting the PIP cycles.

3.2. Geometry of Coolant Passage

A CT scan inspection was carried out to elucidate the geometry of the coolant passages. The CT scan images in the $X-Y$ plane captured by a pitch of 0.02 mm along the Z-axis showed periodic structure for both specimens. Two neighboring CT slice images were shown in Fig. 7(a) and 7(b) for specimen 3D-L, and Fig. 8(a) and 8(b) for specimen 3D-H. The white region in the figures shows high density region (e.g., fiber bundle or matrices), and the dark region shows low density region (e.g., pore).

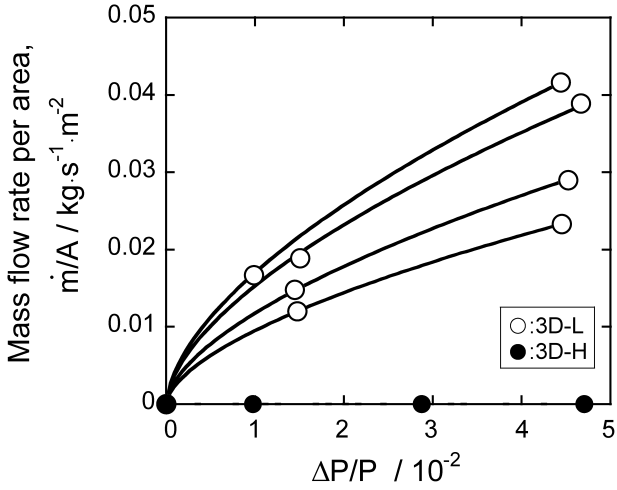

Figure 6. Flow characteristic; data with open symbols were derived from four same lot samples.

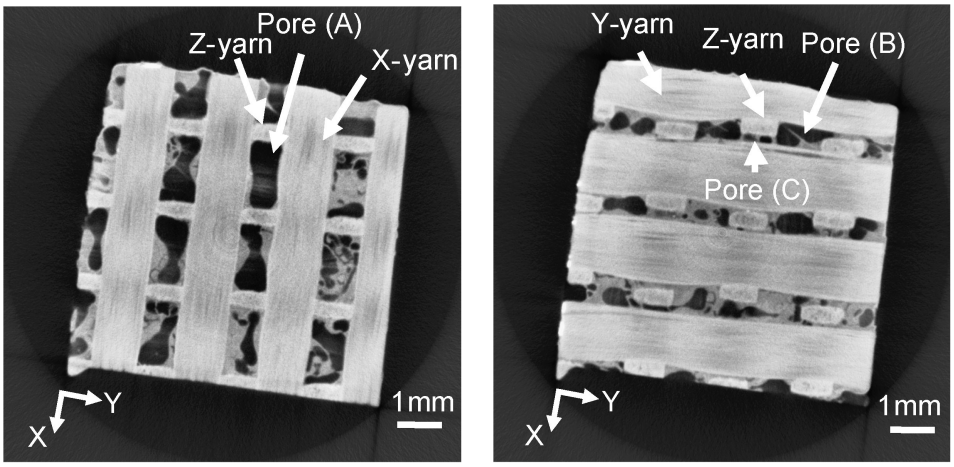

(a) (b)

Figure 7. Micro-focused X-ray CT scan images of the specimen 3D-L showing that the pores A and B are connected by the pore C. (a) 1.06 mm height from the bottom, (b) 1.26 mm height from the bottom.

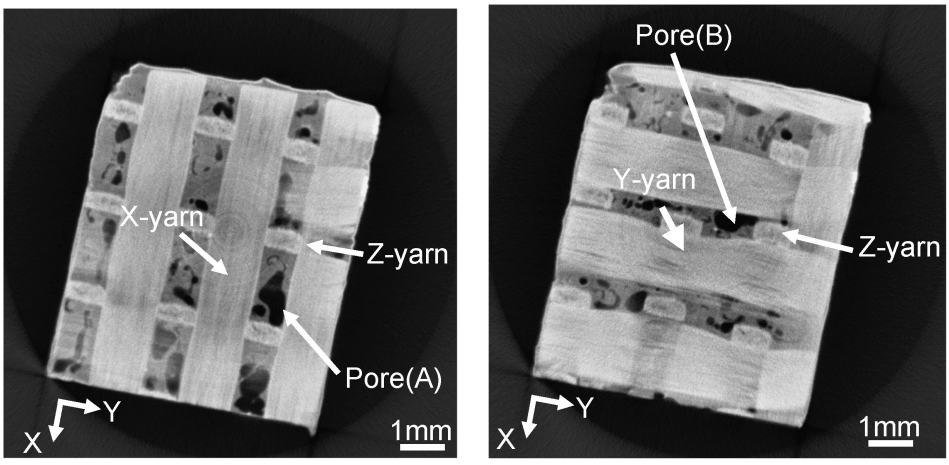

(a) (b)

Figure 8. Micro-focused X-ray CT scan images of the specimen 3D-H showing that the pores A and B have almost no passage to connect them. (a) 0.80 mm height from the bottom, (b) 1.00 mm height from the bottom.

Figure 7(a) indicated that the specimen 3D-L had large pores (A) in the region surrounded by X- and Z-fiber yarns, while Fig. 7(b) showed pores (B) surrounded by Y- and Z-yarns. It can be seen in the figure that the pores (A) and (B) were connected by a pore (C) located near the Z-yarn. Thus, the air passage is formed such as (A)–(C)–(B)–(C)–(A)···. The pore (C) can be considered as a 'throat' region of the air passage which may determine the flow rate of the composite. The areas of the throat regions were measured by computer software that counted pixels in

digital formatted pictures and converted the number of pixels to the area. It was found that the throat area of the pore (C) was significantly scattered in a wide range from 8×10^{-4} to 2×10^{-1} mm^2, which resulted in the scatter of air flow rates. The variation in the throat area should be reduced for a precise control of the air flow.

On the other hand, Fig. 8(a) and 8(b) shows that the PIP–SiC matrix was well deposited to reduce pore size. In addition, the pore that connected the pores (A) and (B) was hardly observed in the specimen 3D-H, because a large amount of PIP–SiC matrix was deposited around the Z-fiber yarn. A space around the Z-fiber yarn should also be a route of penetration of polycarbosilane in the PIP process. The route was almost filled with PIP-matrix after 9 PIP cycles, which indicated that further PIP cycles would not change the internal structure.

3.3. Thermal Fatigue Behavior During Burner Rig Test

The thermal fatigue durability of specimens 3D-L and 3D-H was evaluated under burner heating and air cooling, which simulates the jet-engine operation. Figure 9 shows an overview of the burner rig test (a) and the specimen 3D-L during heating at 200 cycles (b). Both specimens of 3D-L and 3D-H survived 200 cycles without failure.

Temperature profiles during the first cycle ($N = 1$) are shown in Fig. 10, where T_F and T_R are temperatures measured at front-centered and rear-centered and the temperature difference ΔT ($= T_F - T_R$).

The front temperatures T_F of 3D-L and 3D-H increased and saturated to almost the same value of 1230°C during heating. Thus the transpiration cooling effect was not obtained in 3D-L, because the differential pressure cannot be supplied due to the limitation of the burner rig facility. The thermal fatigue property of 3D-L should also be investigated in a test condition with the transpiration cooling effect activated. For the purpose, the testing configuration in future work should be modified.

On the other hand, the rear temperature T_R of 3D-L is slightly lower than 3D-H, that is, the temperature difference ΔT of 3D-L is slightly higher than that of 3D-H.

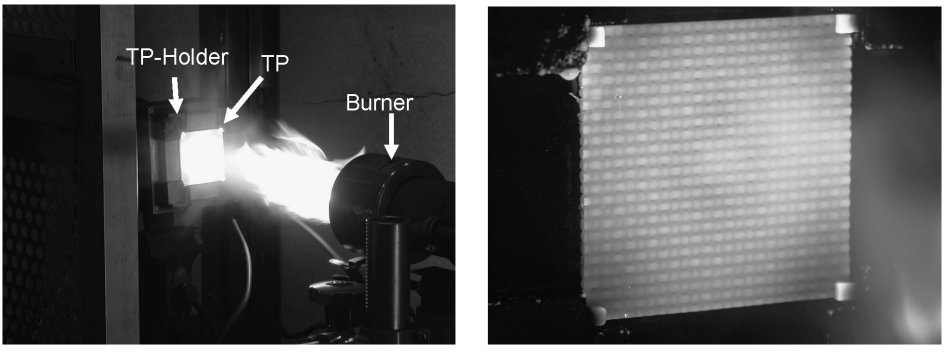

(a) (b)

Figure 9. Burner rig test facility and specimen during the test. (a) Test facility during heating, (b) specimen 3D-L during heating at 200 cycles.

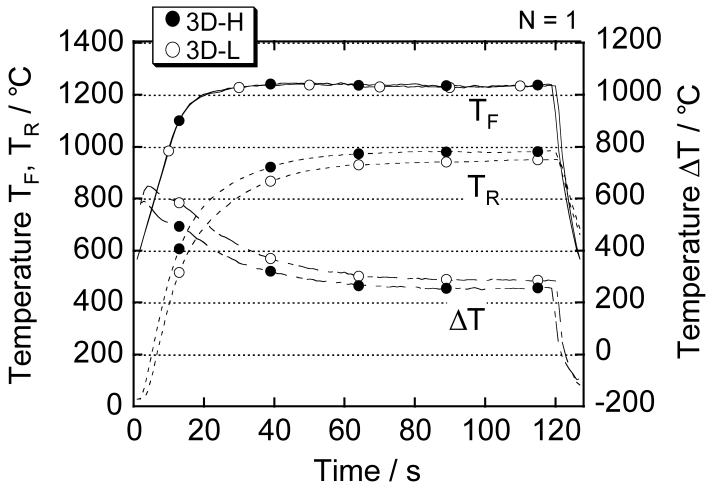

Figure 10. Profiles of the front and back surface temperatures at the center, T_F, T_R, and the temperature difference ΔT $(= T_F - T_R)$ in the first thermal cycle $(N = 1)$.

The temperature difference ΔT under steady state is determined by thermal balance. Under the steady state at $N = 1$, the ratio of heat flux of 3D-L and 3D-H is given by

$$\frac{q_L}{q_H} = \frac{K_L \Delta T_L}{K_H \Delta T_H} = 1.07,$$

where q and K are, respectively, heat flux and thermal conductivity, indicating that the heat flux of 3D-L is 7% higher than that of 3D-H. This may be attributed to the difference in surface morphology. The surface of 3D-L is rougher than 3D-H because of less deposited PIP–SiC matrix. The rough surface would increase the heat transfer coefficient, which results in an increase in heat flux.

The thermal stress ratio of 3D-L and 3D-H can be roughly estimated by the ratio of $E_L \alpha_L \Delta T_L / E_H \alpha_H \Delta T_H = \sim 1.0$. It is suggested that the macroscopic thermal stress of 3D-L nearly equals that of 3D-H.

The histories of the temperatures, T_F, T_R and ΔT at the end of the heating period (after 120 s in each thermal cycle) are shown in Fig. 11. The temperatures T_F, T_R and ΔT of both specimens were found to remain almost constant throughout 200 thermal cycles. The results indicated that the thermal conductivities of both specimens were not significantly changed during 200 cycles, which suggested that a failure that affected thermal conductivity, such as an interlaminar crack, was not generated in both of the specimens.

3.4. Residual Strength

In order to evaluate the strength degradation due to thermal fatigue, the 4-point bending tests were carried out. Figure 12 shows the bending strength measured after 200 thermal cycles and the initial strength obtained from virgin specimens. It can

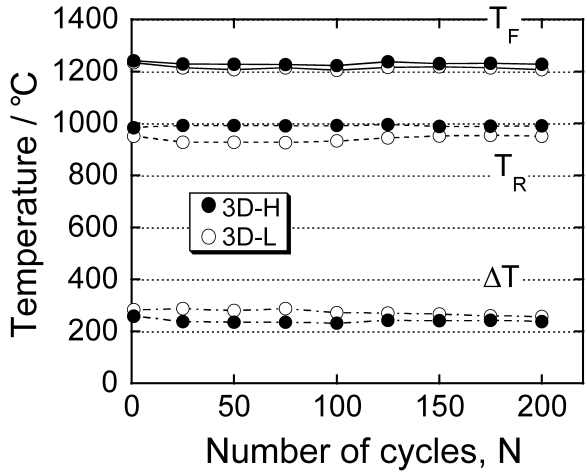

Figure 11. Histories of the front and back surface temperatures at the center T_F, T_R and ΔT $(= T_F - T_R)$ measured at the end of heating period during the thermal cycling.

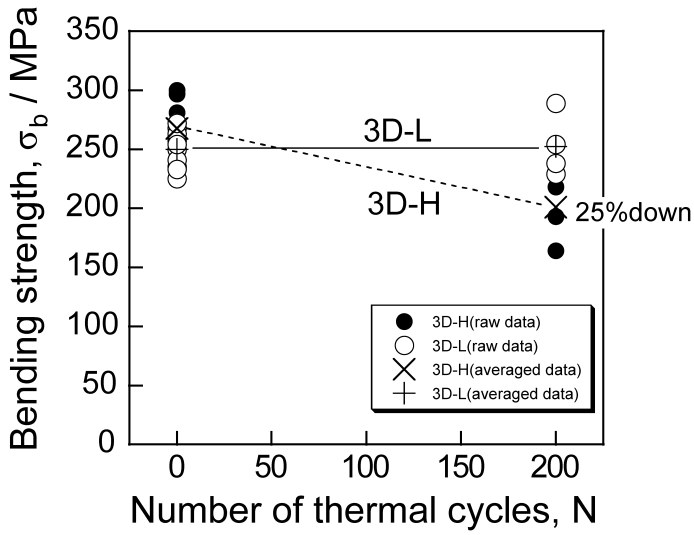

Figure 12. Effect of thermal cyclic loading on the bending strength. Bending strengths at $N = 0$ were obtained by untreated samples.

be seen that even the strengths of untreated specimens are widely scattered, which may suggest that the specimen width should be increased to include more pitches of textures in order to decrease the scatter. The specimen with dense matrix (3D-H) showed a 25% decrease in strength after the thermal fatigue test. On the other hand, the specimens with the porous structure for the transpiration cooling (3D-L) showed almost no decrease in strength following the burner rig test. It is confirmed that the composite with the porous matrix exhibits excellent thermal fatigue property.

The oxidation of the carbon interface coating during thermal cycles can result in a decrease in bending strength of the SiC/SiC composites, because the carbon interface coating is one of dominant factors in determining the strength of the composite. The specimen 3D-L has less PIP–SiC matrix than 3D-H, which may allow more oxygen to be diffused through the matrix and to be delivered to the fiber bundles. This suggests that the specimen 3D-L would be more sensitive to oxidation. Since the specimen 3D-L showed excellent durability after the thermal fatigue test, the oxidation would not be the dominant factor in this thermal fatigue test. In fact, there was no significant difference in the degree of fiber pull-out between specimens 3D-L and 3D-H.

The reason for the excellent properties of 3D-L can be considered to arise in the following way. (1) The porous matrix may decrease thermal stress. For example, a porous matrix results in a decrease in elastic modulus of the matrix. The low elastic modulus decreases elastic constraint on the deformation of the fiber bundle that is induced by thermal contraction during quenching. Thus relaxation of the elastic constraint can decrease thermal stress in the fiber bundle. (2) The large pores in the PIP–SiC matrix of 3D-L may prevent crack propagation from fiber or CVI–SiC matrix in a fiber bundle. In order to clarify the reasons, it is necessary to observe the micro-damages in both of the specimens subjected to the burner rig test.

3.5. Thermal Fatigue Damages

Microscopic observation was carried out to investigate thermal fatigue damages accumulated during the burner rig test. Figure 13 shows an optical micrograph of the polished cross-section at the center of burner-sided surface of 3D-L after 200 thermal cycles. No crack was observed even after 200 thermal cycles. Accordingly, the crack arresting effect of pores was not observed.

On the other hand, Fig. 14 shows a corresponding micrograph of 3D-H after 200 thermal cycles. A few fiber cracks perpendicular to the Y-fiber yarns were observed near the burner-sided surface. Since any cracks in the Y-fiber yarns were not observed in virgin samples, these fiber cracks were induced by thermal stress during thermal cycles. The comparison of Figs 13 and 14 suggests that the porous structure of 3D-L may relax thermal stress and thus prevent from forming cracks. However, it is difficult to specify the number of cycles of the crack initiation by examining the change in temperature difference ΔT, because the direction of the cracks was along thickness and thus the thermal conductivity in thickness direction can be hardly affected by the cracks.

The degradation in bending strength of 3D-H may be attributed to microscopic damages induced during thermal cycles. So it is necessary to investigate the difference in the bending fracture process between 3D-H and 3D-L, which reveals if the thermally-induced damages affect the bending fracture process. The fracture processes of the bending specimens of 3D-H and 3D-L subjected to the burner rig test were considered as follows. The main crack of 3D-L was initiated at fillet-shaped corner where two fiber bundles on tension side were intersected. On the

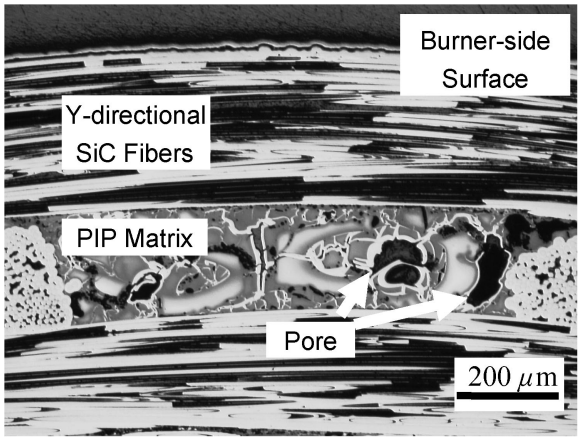

Figure 13. Optical micrograph of polished cross-section at center of burner-side surface of 3D-L tested after 200 thermal cycles showing that no crack was observed.

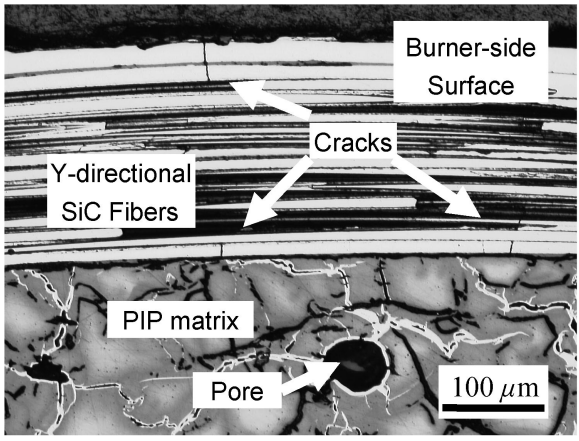

Figure 14. Optical micrograph of polished cross-section at center of burner-side surface of 3D-H tested after 200 thermal cycles showing that a few fiber cracks were formed perpendicular to Y-directional SiC fibers.

other hand, the main crack path of 3D-H was similar to that of 3D-L, which suggested that the thermally-induced fiber cracks did not affect the initiation of the main crack during bending. Since the fiber cracks necessarily increase tensile stress on the undamaged fibers, the fiber cracks may indirectly affect the propagation of the main crack. However, the microscopic damages in the fractured bending specimens are so complicated that the interaction between the fiber damages and the bending fracture process cannot be clarified, which suggests that further investigation of the detail fracture process is needed.

Further study is needed to clarify the mechanisms of the enhancement of durability due to high porosity, which is indispensable to develop the SiC/SiC composites with higher thermal fatigue durability.

4. Conclusions

The transpiration cooling structure was fabricated in the SiC/SiC composite with the porous matrix. Burner rig tests were conducted to evaluate the thermal fatigue behavior of the composites. The effects of the porous structure on the strength degradation due to thermal fatigue were investigated in comparison with the composites with the dense matrix, and the following conclusions were obtained.

(1) The coolant passage created in the composite with the porous matrix is revealed by micro-focused X-ray CT scan. The throat region, which may be dominant for the flow characteristics, was located in small pores near the Z-fiber yarn.

(2) The SiC/SiC composite with the dense matrix showed a decrease in strength of 25% after 200 thermal cycles in the thermal fatigue tests. In contrast, the composite with the porous matrix showed almost no strength degradation after the thermal fatigue test. Thus the composite with the porous matrix showed excellent thermal fatigue durability.

(3) Microscopic observation revealed that cracks induced by thermal stress were formed near the burner-sided surface in the dense matrix composites during thermal fatigue test, but that no cracks were observed in the porous composite. The excellent durability of the porous matrix composites may be attributed to the thermal stress relaxation due to porous structure.

Acknowledgements

The author would like to acknowledge the efforts of Sunao Sugimoto of Japan Aerospace Exploration Agency (JAXA) for his aid in measurements with the Micro-focused X-ray CT scan.

References

1. B. N. Cox, J. B. Davis, D. B. Marshall and Q. D. Yang, Integral textile ceramic composites for turbine engine combustors, in: *Proc. ASME TURBO EXPO 2002*, ASME GT-2002-30056 (2002).
2. A. H. Lefebvre, *Gas Turbine Combustion*, 2nd edn, pp. 298–299. Taylor and Francis Ltd., London (1999).
3. R. M. Orenstein and D. J. Green, Thermal shock behavior of open-cell ceramic forms, *J. Amer. Ceram. Soc.* **75**, 1899–1905 (1992).
4. R. Brezny and D. J. Green, Fracture behavior of open-cell ceramics, *J. Amer. Ceram. Soc.* **72**, 1145–1152 (1989).
5. J. She, T. Ohji and Z. Y. Deng, Thermal shock behavior of porous silicon carbide ceramics, *J. Amer. Ceram. Soc.* **85**, 2125–2127 (2002).

6. T. Araki, K. Watanabe, T. Yoshida, S. Nishide and S. Masaki, High temperature properties of SiC fiber reinforced SiC matrix composites for turbine rotor application, *Ceram. Engng. Sci. Proc.* **23**, 581–588 (2002).
7. S. Sugimoto, T. Aoki, Y. Iwahori and T. Ishikawa, Non-destructive evaluation of composites using micro-focused X-ray CT scanner, *AIP Conf. Proc.* **760**, 1081–1086 (2005).